Journal of Alloys and Compounds 844 (2020) 155875

Contents lists available at ScienceDirect

Journal of Alloys and Compounds

journal homepage: http://www.elsevier.com/locate/jalcom

Engineering mixed polyanion red-emitting $Rb_2Bi(PO_4)(WO_4):Eu^{3+}$ phosphors with negligible thermal quenching and high quantum yield

Zhen Jia [a, **], Xiuling Zhang [a], Xiaoying Hua [a], Yan Dong [a], Hongliang Li [a], Chuanqi Feng [a], Yonggang Wang [c], Mingjun Xia [b, *]

[a] College of Chemistry and Chemical Engineering, Dezhou University, Dezhou, 253023, PR China
[b] Beijing Center for Crystal Research and Development, Key Laboratory of Functional Crystals and Laser Technology, Technical Institute of Physics and Chemistry, Chinese Academy of Sciences, Beijing, 100190, PR China
[c] Center for High Pressure Science & Technology Advanced Research, Beijing, 100094, PR China

ARTICLE INFO

Article history:
Received 3 April 2020
Received in revised form
27 May 2020
Accepted 30 May 2020
Available online 21 June 2020

Keywords:
$Rb_2Bi(PO_4)(WO_4):Eu^{3+}$
Red-emitting
High quantum yield
Negligible thermal quenching

ABSTRACT

The high-performance red-emitting phosphors are strongly demanded as the next generation solid state lighting materials. Benefitting from the favorable accommodation capacity of polyanions and high charge transfer energy state in the structure, the pure red-emitting $Rb_2Bi(PO_4)(WO_4):Eu^{3+}$ (RBPWO:Eu^{3+}) materials with negligible thermal quenching and high quantum yield were synthesized. RBPWO:Eu^{3+} has high absolute quantum yields of 88.1% and exceptional thermal stability of 98.6% integral retention at 423 K relative to the initial value at 298 K. Additionally, affected by the low symmetry crystalline-field of D_{2h}, the title phosphors exhibit intense absorption band peaking at 394 nm and pure red light with the color CIE values (0.6482, 0.3515). The white light-emitting diode (*w*-LED) device fabricated from the title material exhibits low correlated color temperature (4000 K), high color rendering index (R_a = 90) and moderate luminous efficiency (18.07 lm/W) in the preliminary experiment. The present work indicates that the RBPWO:Eu^{3+} phosphors are promising red components for the near ultraviolet light excited *w*-LEDs.

1. Introduction

White light-emitting diodes (*w*-LEDs) are widely used in indoor and outdoor illumination due to the low energy consumption, high brightness, long working life and environmental friendliness [1–3]. The popular implementation approach for fabricating commercial *w*-LEDs is coating the yellow $Y_3Al_5O_{12}:Ce^{3+}$ (YAG:Ce^{3+}) materials on the blue-emitting InGaN chips [4–8]. However, they suffer from an insufficient color rendering index (R_a) and high correlated color temperature (T_c) [9]. To reach the high-quality white light, a promising solution was developed: utilizing the near ultraviolet (NUV) light to pump the three primary colors (blue, green and red) phosphors [10–13]. The driver for such applications has involved the extensive exploration for high-performance red-emitting materials matched with the NUV light emitting chips.

To date, several commercial red phosphors including $Sr_2Si_5N_8:Eu^{2+}$ [14], (Sr,Ca)$AlSiN_3:Eu^{2+}$ [15], $Y_2O_3:Eu^{3+}$ [16] and $Y_2O_2S:Eu^{3+}$ [17] have been developed. Although the $Sr_2Si_5N_8:Eu^{2+}$ [14] and (Sr,Ca)$AlSiN_3:Eu^{2+}$ [15] materials possess broad band emission, their luminous efficacies are influenced due to a portion of the spectra located in the eye-insensitive region (above 700 nm). Additionally, the synthesis of bivalence europium based materials requires a reducing atmosphere, which results in the higher production costs [18–20]. It seems that the Eu^{3+} ion is a promising activator because of its narrow red line emission. However, the $Y_2O_2S:Eu^{3+}$ materials are easily deliquescence to release toxic sulfide gases and their service lives are reduced. In general, metal oxide compounds have excellent thermal stability. For example, the melting point of Y_2O_3 is over 2000 °C. The Eu^{3+} doped Y_2O_3 phosphors have intense absorbance centred at 255 nm in UV region, but they can't effectively be excited by NUV light [21]. Among the emission bands of Eu^{3+}, only the $^5D_0$-$^7F_2$ transition is responsible for the typical red luminescence emission. In view of the luminescence behaviors of Eu^{3+} are susceptible to their crystallographic environments, designing good structure of the matrix is

* Corresponding author.
** Corresponding author.
E-mail addresses: jiazhen@mail.ipc.ac.cn (Z. Jia), xiamingjun@mail.ipc.ac.cn (M. Xia).

https://doi.org/10.1016/j.jallcom.2020.155875
0925-8388/

vital [22–25]. First of all, the excellent accommodation capacity for Eu^{3+} ions is essential. Based on the Vegard Law, if the radii values difference of two metal ions is within 15%, they can be replaced each other easily [26]. Among the eight-coordinated trivalent metal ions, including Sc^{3+}, Y^{3+}, La^{3+}, Gd^{3+}, Lu^{3+} and Bi^{3+}, the radius difference of Gd^{3+} or Bi^{3+} and Eu^{3+} is less than five percent. Therefore, the gadolinium or bismuth based compounds are considered as suitable host compounds [27]. In addition, the existence of concentration quenching effect results in the limited content of activators ions, which will lead to insufficient fluorescence quantum yields [28,29]. For instance, the critical quenching contents (x_c) of Eu^{3+} in $CaGdAlO_4$:Eu^{3+} and Ba_2YAlO_5:Eu^{3+} are 7 mol % and 30 mol %, respectively [29]. Some large anionic groups such as PO_4 and WO_4, can segregate the adjacent luminescence activators that contribute to reducing the interaction between adjacent europium ions and increasing luminous particles density. The x_c values in $Ca_9Bi(PO_4)_7$:Eu^{3+} and $NaSrLa(WO_4)_3$:Eu^{3+} are 60 and 80 mol %, respectively [30,31]. Based on Binnemans theory, the $^5D_0$-$^7F_2$ transition of Eu^{3+} is hypersensitive for the crystallographic surroundings and the low symmetry host structure is beneficial for strengthening the $^5D_0$-$^7F_2$ transition [24,32].

Herein, the $Rb_2Bi(PO_4)(WO_4)$:Eu^{3+} (RBPWO:Eu^{3+}) materials were investigated. In the structure of RBPWO:Eu^{3+}, the mixed polyanions PO_4 and WO_4 coexist and the Eu^{3+} ions can easily substitute Bi^{3+} at any Eu^{3+}/Bi^{3+} ratio, and the x_c is capable to reach 90%. Meanwhile, the high absolute quantum yields (AQY) of 88.1% was obtained. In addition, RBPWO belongs to orthorhombic system, thus its low symmetry structure of D_{2h} makes the $^5D_0$-$^7F_2$ transition of Eu^{3+} very intense and dominating the emission spectrum [32]. The thermal stability of trivalent europium doped materials relies heavily on the charge-transfer (CT) state of Eu^{3+}. Blasse considered that the electrons can absorb thermal energy and then jump to the CT state. Afterwards, they return to ground state directly without emitting light [33]. Obviously, the phosphors with the high-level CT states should exhibit high quenching temperature and good thermal stability. In RBPWO:Eu^{3+}, the highly positioned CT energy level (260 nm) of Eu^{3+} was observed, and the exceptional thermal stability of the phosphors was obtained that is 98.6% integral retention at 423 K relative to the initial value at room temperature. Thereby, the red-emitting phosphors RBPWO:Eu^{3+} have pure color, good thermal stability and high quantum efficiency. This high-efficiency red light emission phenomenon can be observed in other $Rb_2Bi(PO_4)(WO_4)$-type phosphors containing mixed polyanion, such as $Na_2Gd(PO_4)(MoO_4)$ and $Na_2Lu(PO_4)(MoO_4)$ [34–38]. Herein the site occupancy, optical properties, heat resistance properties, AQY and the potential application of RBPWO:Eu^{3+} were systematically studied.

2. Experimental

2.1. Material synthesis

The $Rb_2Bi(PO_4)(WO_4)$:xEu^{3+} (RBPWO:xEu^{3+}) ($0 \le x \le 1$) materials were prepared by the solid state reaction in the air atmosphere. The stoichiometric amounts of Rb_2CO_3 (99%, Macklin Co., Ltd), Bi_2O_3 (99.9%, Macklin Co., Ltd), $NH_4H_2PO_4$ (99%, Macklin Co., Ltd), WO_3 (99.5%, Macklin Co., Ltd) and Eu_2O_3 (99.99%, Shanghai Yuelong Rare earth New Materials Co., Ltd) were mixed thoroughly and preheated at 500 °C for 12–36 h. Subsequently, the mixture was sintered at 700 °C for 48 h with 3–5 intermediate grindings.

2.2. Characterization

The crystal structures were characterized with use of a Bruker D8 Advance X-ray diffractometer. The scanning step was 0.05 $^o s^{-1}$. The structure was refined by the General Structure Analysis System (GSAS) and the EXPGUI software [39,40]. The morphology of the samples were observed by a field emission scanning electron microscope (MERLIN Compact, SEM). The optical diffuse reflectance spectra (DRS) were recorded on a Varian Cary 5000 spectrophotometer. The room-temperature and variable-temperature photoluminescence (PL), photoluminescence excitation (PLE) spectra and luminescence lifetimes were taken by an FLS-980 spectrofluorometer. The optical properties of fabricated *w*-LED device were measured by an Everfine LED instrument. The absolute quantum yields (AQY) were measured using an integrated sphere device according to the equation (1):

$$AQY = \frac{L_{Sample}}{E_{Reference} - E_{Sample}} \quad (1)$$

Where, L_{Sample} is the emission integrals of samples, $E_{Reference}$and E_{Sample} stand for the scatter integrals of the samples and the reference (a white tablet pressed by the $BaSO_4$ powders).

3. Results and discussion

3.1. Rietveld refinement and phase identification

To check the structure of the as-synthesized RBPWO:xEu^{3+} compounds, the crystal data RBPWO (ICSD# 426594) was adopted as an initial refinement model [32]. The observed and calculated XRD patterns for RBPWO and Eu^{3+} completely substituted compound $Rb_2Eu(PO_4)(WO_4)$ are shown in Fig. 1. The final agreement factors converged to $R_p = 7.94\%$ and $R_{wp} = 10.34\%$ for RBPWO, $R_p = 7.86\%$ and $R_{wp} = 9.94\%$ for $Rb_2BiEu(PO_4)(WO_4)$, which verify the two compounds were synthesized successfully [41,42]. Additionally, in Fig. 2a, the diffraction curves are given for selected compositions and they match well with the pattern of matrix compound that verifies the successful incorporation of Eu^{3+} ions into the host structure.

3.2. Micro-morphology

The morphologies of the RBPWO, RBPWO:$0.9Eu^{3+}$ and $Rb_2Eu(PO_4)(WO_4)$ compounds are presented in Fig. 3 and they are analogous. The samples comprised the plate-like particles with the size range of 0.5–4 μm. The faceted plate-like particle morphology is an indicator of layered crystal structure, similar relation was observed in other crystal family of layered molybdates [43–45]. The strongly heterogeneity is stemming from the manual grinding after calcination. Meanwhile, the surface of the particles is clean and smooth, indicating the materials are highly crystallized and that is beneficial to realize the high light output.

3.3. Crystal structure and preferable site occupancy

The RBPWO compound crystallizes in a centrosymmetric lattice with the space group of *I*bca. In the RBPWO structure, each cation (Rb^+, Bi^{3+}, P^{+5} and W^{+6}) has a unique crystallographic position [32]. Both Rb and Bi atoms are eight-coordinated to form the RbO_8 and BiO_8 dodecahedra, while P and W atoms are connected to four O atoms in forming the PO_4 and WO_4 tetrahedra (Fig. 4a). Along the *b* direction, BiO_8 and PO_4 polyhedron are combined to construct a two-dimensional $^2_\infty(Bi_2P_2O_{12})^{8-}$ chain (Fig. 4b). Further, the WO_4 tetrahedra are attached in both sides of the chain by sharing the O atoms of BiO_8 polyhedron, with Rb atoms occupying the voids between the neighbouring sheets.

As based on Shannon empirical relations, the ionic radii of eight-coordinated Rb^+, Bi^{3+} and Eu^{3+} are 1.60, 1.11 and 1.07 Å, and those

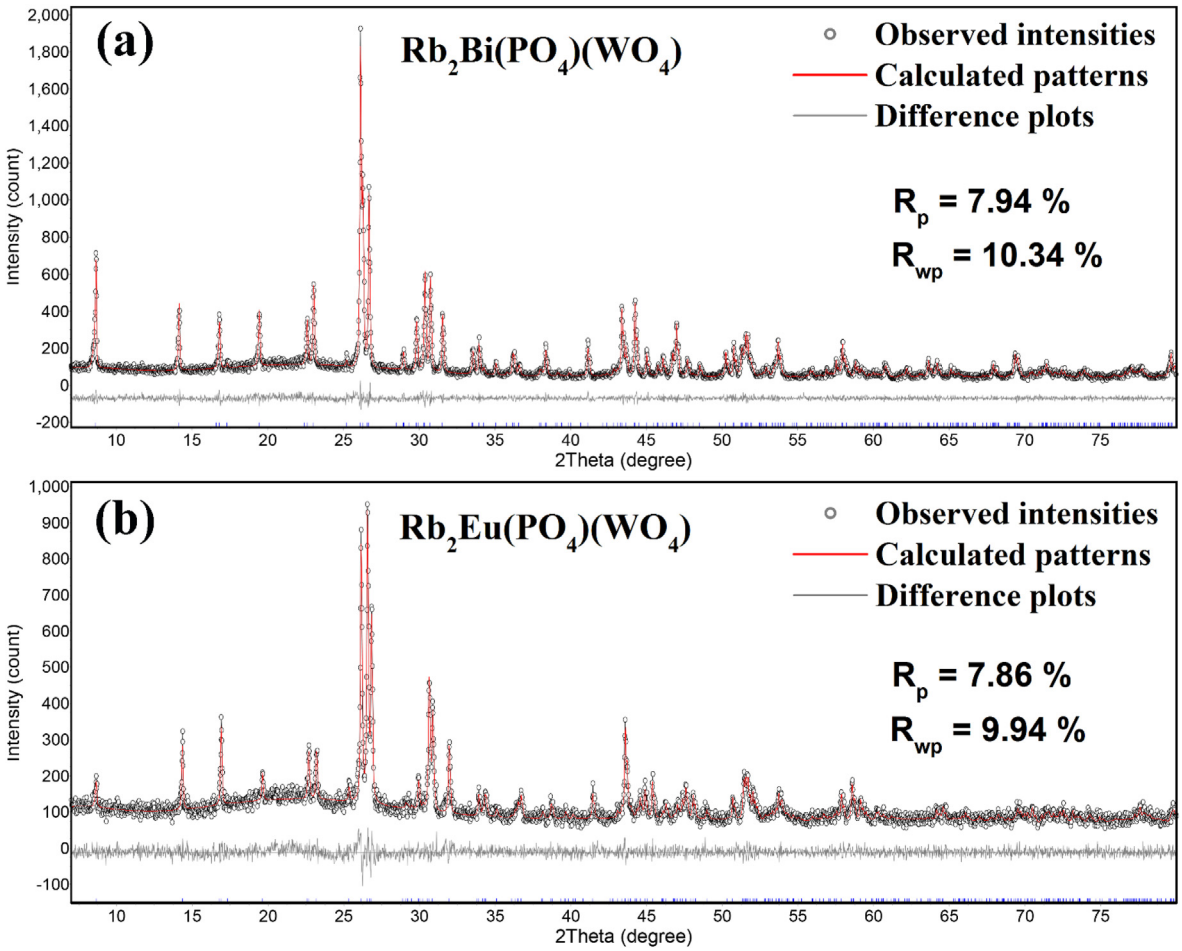

Fig. 1. Rietveld structure refinement plots for (a) RBPWO and (b) $Rb_2Eu(PO_4)(WO_4)$.

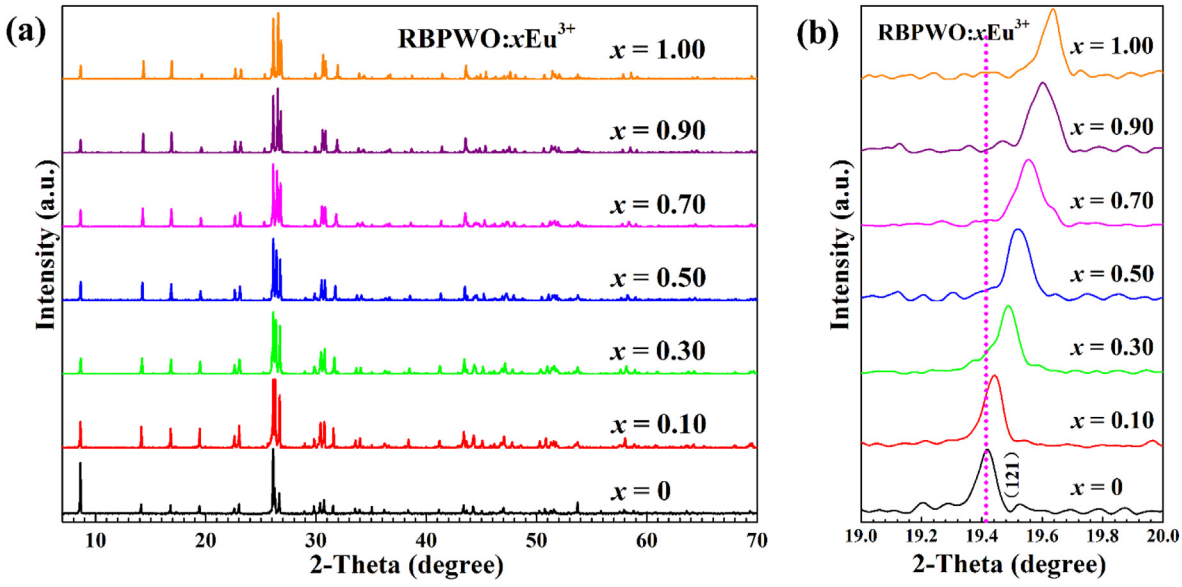

Fig. 2. (a) The representative XRD patterns, and (b) the magnified XRD patterns with the selected diffraction peaks from 19° to 20° of RBPWO:xEu^{3+} ($0 \leq x \leq 1$).

of four-coordinated P^{5+} and W^{6+} cations are 0.31 and 0.42 Å, respectively [27,46,47]. Apparently, compared to Eu^{3+}, Rb^{+} is too large, while P^{5+} and W^{6+} are too small, and only the size of Bi^{3+} is very close to that of Eu^{3+}. Therefore, the trivalent europium ions are mostly likely occupying the lattice sites of Bi^{3+}. Besides, the large valence difference between the cations is further factor to exclude

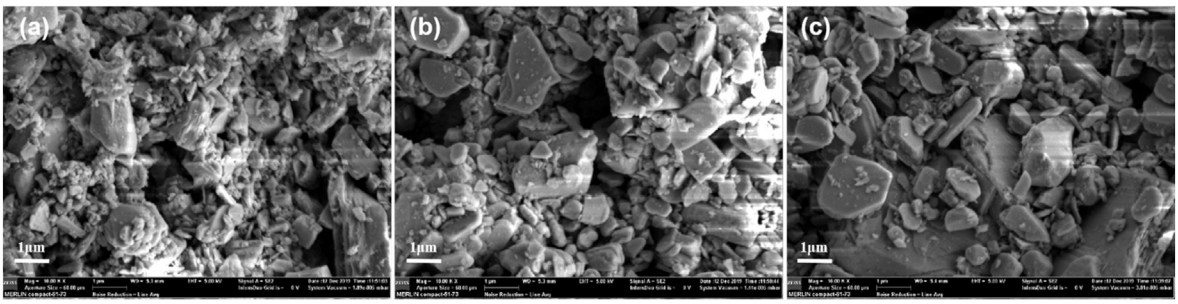

Fig. 3. SEM images for (a) RBPWO, (b) RBPWO:0.9Eu^{3+}, and (c) $Rb_2Eu(PO_4)(WO_4)$.

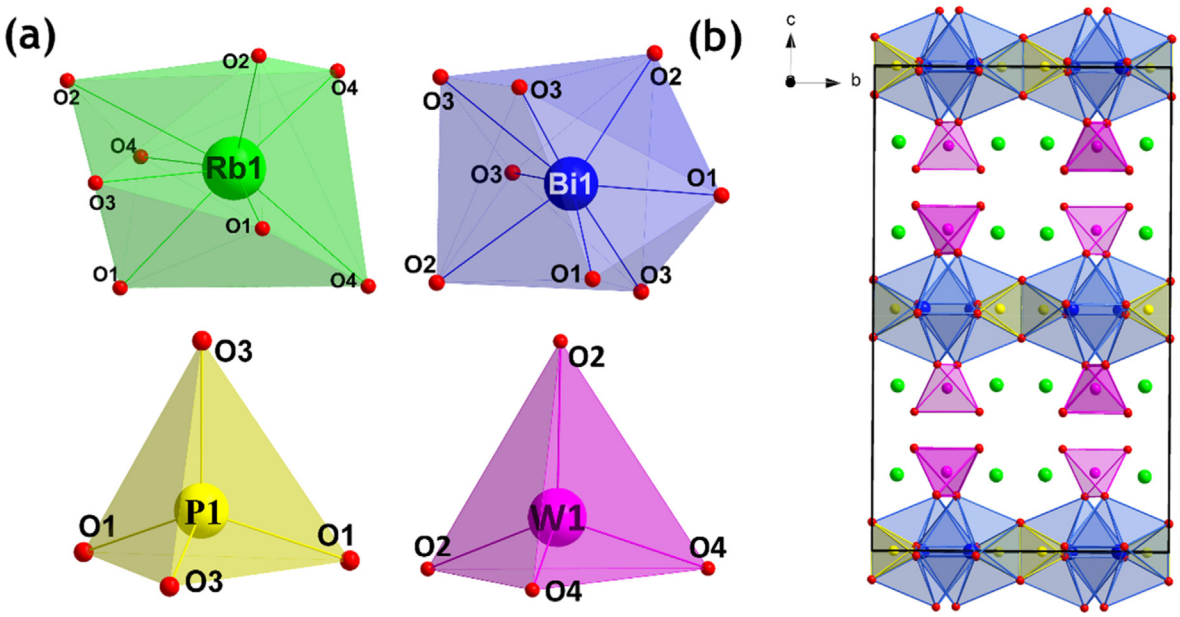

Fig. 4. (a) Coordination environments of cations and (b) crystal structure of RBPWO viewed along *a* axis.

the trivalent europium ion substitution for monovalent rubidium, pentavalent phosphorus or hexavalent tungsten ions. The representative diffraction peak of RBPWO:*x*Eu^{3+} ($0 \le x \le 1.00$) appeared in the diffraction angle range from 19° to 20° is shown in Fig. 2b. Clearly, the characteristic peak (121) shifts gradually to higher angles with the Eu^{3+} content increase. This is derived from the eight-coordinated Eu^{3+} is slightly smaller than the same-coordinated Bi^{3+} [27,46,47]. The decay curves of the RBPWO:Eu^{3+} substances, as given in Fig. S1, match well with a single-exponential function and it further shows that Eu^{3+} occupy only unique Bi^{3+} crystallographic site.

Based on Vegard Law, if the radii values difference of Bi^{3+} and Eu^{3+} cations is within 15%, Eu^{3+} can be dissolved into the host to form a solid solution [26]. Since the size difference of Bi^{3+} and Eu^{3+} cations is about 3.6%, the formation of wide-range RBPWO:*x*Eu^{3+} solid solutions can be predicted. As seen in Figs. 1 and 2, the Eu^{3+} ions can substitute Bi^{3+} ions at any Eu^{3+}/Bi^{3+} ratio without phase transition that is in good relation with the prediction. The structure of RBPWO is quite flexible for the incorporation of doped Eu^{3+} ions, and the RBPWO:Eu^{3+} materials can be easily obtained in pure polycrystalline form.

The cell parameters of RBPWO:*x*Eu^{3+} compounds reduced linearly as the content of Eu^{3+} increased, as shown in Fig. 5 and Table S1. Intriguingly, the reduction rates of the cell parameters are different: *b* shows the maximum slop of 0.1714, followed *a* (0.0397), and *c* has a minimum value (0.0156). The results are closely related to the matrix structure. As shown in Fig. 4b, the BiO_8 dodecahedra are ordered as layer-structure along *a*, *b* and *c* directions, connecting with RbO_8, PO_4 and WO_4 to form the three-dimensional (3D) network. However, the inter-lamellar distances of BiO_8 layers are quite different along the different crystallographic orientation (Fig. 6). Along *c*-axis, the interlayer distance is as large as 10.23 Å (Fig. 6c), and it is only 3.53 Å (Fig. 6a) along *a*-axis and 2.09 Å (Fig. 6b) along *b*-axis which is the shortest value [32]. Therefore, with the minimum (Bi, Eu)O_8 layer distance, the cell parameter *b* is very sensitively to the variation of average ion size. This is another evidence as the Eu^{3+} ions are successfully doped into the RBPWO host lattice.

3.4. UV-visible DRS and photoluminescence properties

$$\alpha \Big/ S = F(R) = (1-R)^2 \Big/ 2R \qquad (2)$$

Where α, S and R are the absorption, scattering and reflectance coefficients, respectively. As seen in **Fig. 7(a and c),** the transitions in the DRS curve are the same as those of the PLE spectrum of RBPWO:0.9Eu^{3+}. However, their relative intensities are very

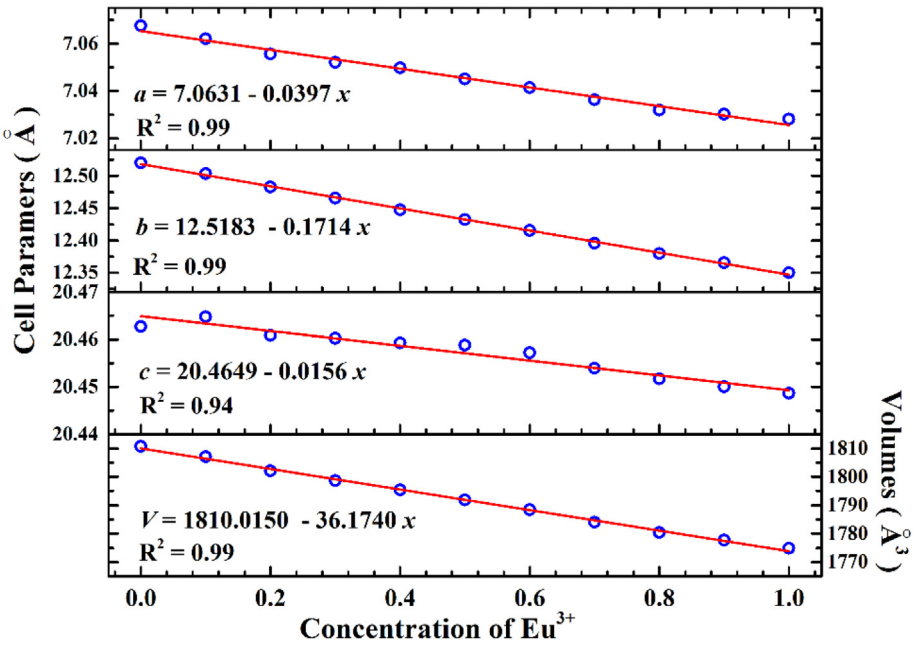

Fig. 5. Cell parameters variation in the RBPWO:xEu^{3+} ($0.01 \leq x \leq 1.0$) compounds.

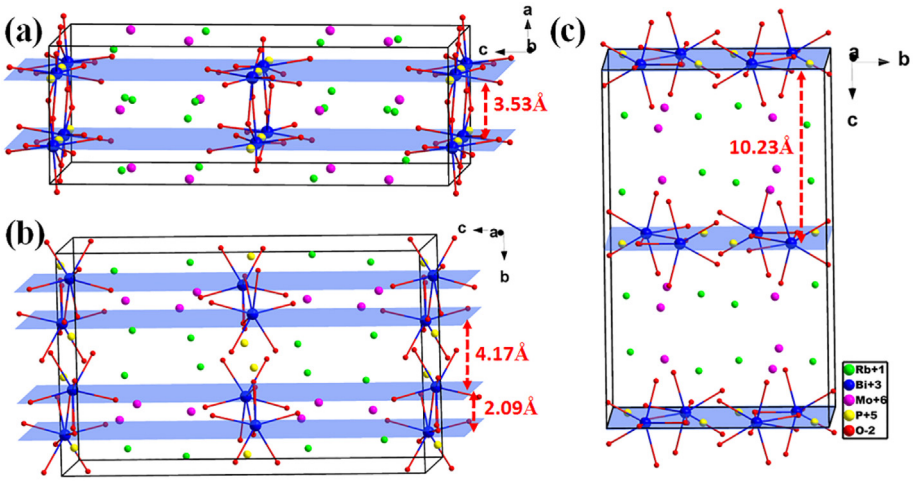

Fig. 6. Crystal structure of RBPWO with the planar $[BiO_8]_\infty$ layer along a, b and c directions.

different because the excitation transitions are also influenced by the QY of the correlative transitions [24]. Only the absorption generating efficient luminescence can be observed in the PLE spectrum. In the ultraviolet region (<350 nm), the very intense absorption bands are originated from the host lattice in DRS spectra. Whereas, the broad bands without fine structure are observed in PLE spectrum. As we all known, the Eu^{3+} ion is inclined to receive one electron from neighbouring oxygen atom to achieve the half-filled electron configuration of Eu^{2+}, and the according absorption transitions are called charge-transfer bands (CTB) [24,26,49]. Whereas, the CTB is inconspicuous in DRS curve for the overlap of the absorption of the host and the CTB of RBPWO:0.9Eu^{3+}. In the NUV region (>350 nm), both DRS and PLE curves of the RBPWO:0.9Eu^{3+} sample show several sharp absorption bands which can be assigned to the transitions from $^5F_0$ to the excitation states of Eu^{3+} ions. In the PLE spectrum, the $^7F_0 \rightarrow {}^5L_6$ transition has the most intense absorption.

The room-temperature luminescence spectrum of RBPWO:Eu^{3+} is the result of the radiative transitions from $^5D_0$ level to the ^7F manifold radiative transitions (**Fig. 7c**), and the $^5D_0 \rightarrow {}^7F_1$ and $^5D_0 \rightarrow {}^7F_{0,\,2,\,4,\,5}$ bands belong to the magnetic and forced electric dipole transitions, respectively [20,50–52]. As it is known, the $^5D_0$-$^7F_2$ transition of Eu^{3+} is responsible for the typical red luminescence emission, however, it is hypersensitive for the crystallographic surroundings [24,53]. In RBPWO:Eu^{3+} compound, the low symmetry structure D_{2h} of the host makes the $^5D_0$-$^7F_2$ transition very intense and dominating the emission spectrum [32]. Meanwhile, the image (**Fig. 7a, inset**), the calculated emission CIE coordinates (0.6482, 0.3515) (**Fig. 7b**) and the high color purity (91%) further illustrate that the red-emitting material has been successfully obtained [54,55].

Additionally, as based on the Judd–Ofelt theory, the $^5D_0 \rightarrow {}^7F_0$ and $^5D_0 \rightarrow {}^7F_3$ transitions are forbidden. In the emission spectra, $^5D_0 \rightarrow {}^7F_0$ emission band is not observed, however, the weak

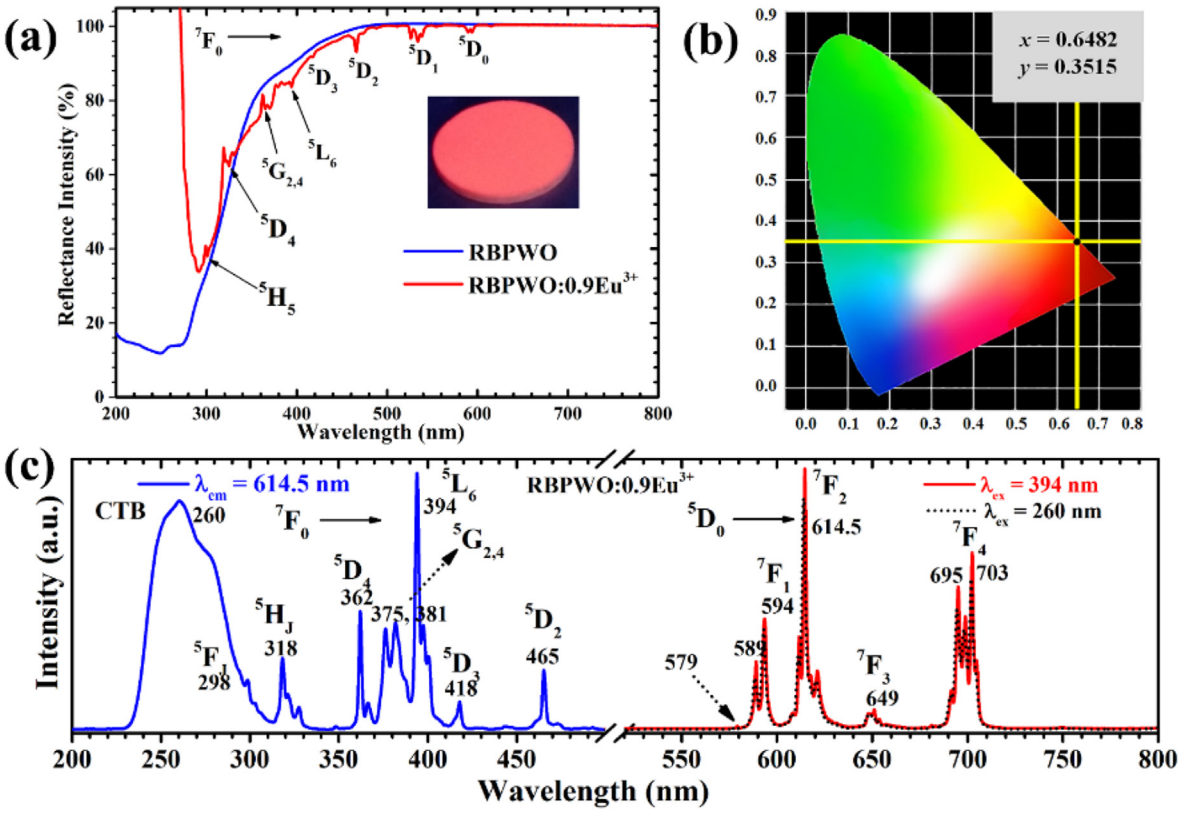

Fig. 7. UV-visible DRS of RBPWO and RBPWO:0.9Eu^{3+} (inset shows the photograph of the RBPWO:0.9Eu^{3+} tablet under the 365 nm excitation light) (a), the CIE color diagram (b) and the PLE and PL spectra of RBPWO:0.9Eu^{3+} (c). The qualitative UV-visible DRS can be obtained according to the function (2) [48].

emission of $^5D_0 \rightarrow {}^7F_3$ is present in the range of 645–660 nm. The anomalous behavior can be explained by the *J*-mixing induced by the crystal-field perturbation [56]. The $^5D_0 \rightarrow {}^7F_1$ transition is split into three sublevels due to the crystal field degeneracy [24]. The emission peaks at 589 nm and 594 nm are explicit, and, however, the one at 579 nm is very weak and almost invisible. Meanwhile, the $^5D_0 \rightarrow {}^7F_4$ emission is weaker than the $^5D_0 \rightarrow {}^7F_2$ emission, but it is more intense than the $^5D_0 \rightarrow {}^7F_1$ and $^5D_0 \rightarrow {}^7F_3$ transitions.

Obviously, the $^5D_0 \rightarrow {}^7F_2$ transition luminescence intensity (Fig. S2), the PL decay times (Fig. S3) and the AQY values (Fig. 8a, Table S3) all increase with the increasing of Eu^{3+} content, and they reach the maximum values $x = 0.9$. Only when the Bi^{3+} ions are completely substituted by Eu^{3+} ions, the luminescence intensity decreased slightly. The critical distance (R_c) between the adjacent Eu^{3+} ions can be calculated by the formula (3) [57]:

$$R_C \approx 2\left(\frac{3V}{4\pi x_c N}\right)^{1/3} \quad (3)$$

Where V, x_c and N are the unit cell volume, critical quenching concentration and the number of Bi^{3+} sites in the unit cell, respectively. In the structure of RBPWO, the unit cell volume is equal to 1810.69 Å and N = 8. When $x_c = 0.9$, the R_c value for concentration quenching is calculated to be 7.83 Å. It is very larger

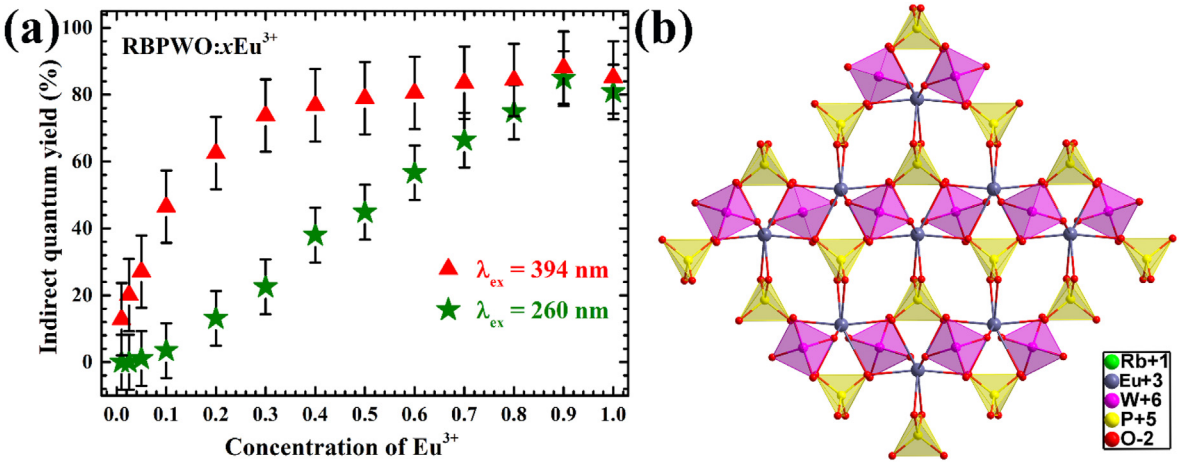

Fig. 8. The absolute quantum yields of RBPWO:xEu^{3+} ($0 < x \leq 1.0$) with 260 nm and 394 nm as excitation wavelength, respectively (a), and the coordination environment of Eu^{3+} (b).

than the minimal interlamellar distance between BiO_8 layers (2.09 Å) (Fig. 6b). This result can be explained by the coordination environment of Eu^{3+}. As shown in Fig. 8b, each Eu^{3+} ion is surrounded by four PO_4 and two WO_4 tetrahedra. The adjacent luminescence activators are segregated by the above mentioned anions groups, which results in the very small interaction between europium ions and the concentration quenching is negligible [30,58,59]. Accordingly, the highest AQY values for the 394 and 260 nm excitation are 88.1% and 84.8%, respectively (Fig. 8a). The 394 nm is very close to the NUV output light of the commercial InGaN chip (395 nm).

3.5. Thermal quenching properties

In general, the working current of modern *w*-LEDs is beyond 350 mA, and the internal temperature of the devices is about 423 K. To realizing the favorable color rendering index, the luminesce stability of the phosphors is essential. For the RBPWO:0.9Eu^{3+} sample, the position of emission maximum peak keeps constant with increasing the environment temperature, which is beneficial for the stability of the color purity (Fig. 9a). Apparently, in higher temperature, the luminesce intensity of 614.5 nm red emission peak decreased gradually, and at 423 K, it decays to 79.7% of the initial value at 298 K (Table S4). As it was considered by Blasse, the charge-transfer state of Eu^{3+} had a significant impact on the luminescence thermal quenching process [33]. As depicted in Fig. 9b, the $^5D_0$ ground and the CTB states of Eu^{3+} are intersect at point S with the energy difference of E_a. At room temperature, the transitions from the excited state $^5D_0$ to the ground state ^7F_J (J = 0–6) result in the emission spectrum. With the ambient temperature increases, when sufficient energy is provided by the thermal energy, the electrons located in $^5D_0$ can jump to the CTB state. During this process, the electron must overcome the energy barrier E_a, which is called activation energy. Then through the intersection S of CTB and $^7F_0$, the electrons located at the CTB state return to ground state directly. However, the transition is non-radiative and does not make contributions to the luminescence, which results in the quenching of luminescence. Based on the mechanism, it can be supposedly that, if the value of E_a is very high, the quenching of luminescence will occur at very high temperature. The activation energy E_a can be calculated from the following equation (4) [60].

$$I_T = \frac{I_0}{1 + Ce^{-E_a/kT}} \quad (4)$$

Where I_0 and I_T stand for the luminescence intensity at 614.5 nm at 298 K and a given temperature T, C is a constant, k is the Boltzmann constant (8.629 × 10^{-5} eV K^{-1}). As shown in Fig. S4, the ln[(I_0/I_T) −1] and 1/kT have a linear relationship, and the slope determines the activation energy E_a to be 0.23 eV.

Interestingly, while the emission intensity at 614.5 nm decrease, the emission lines were broaden due to the increasing of the electron-phonon interaction between the electrons and the lattice vibrations (Fig. 9a, inset) [61]. Due to the electron-phonon interaction, the emission lines blow 423 K in the RBPWO:0.9Eu^{3+},are broaden, which compensates the reduced emission intensity [61]. Therefore, the emission integrals are almost invariably within 423 K (within 1.5%) (Fig. S5 and Table S4), indicating that the total emission outputs change little with increasing temperature.

3.6. Electroluminescence of the fabricated w-LED device

To evaluate the potential application in solid lightings, a *w*-LED device was fabricated by coating the RBPWO:0.9Eu^{3+} phosphor, the commercial blue $BaMgAl_{10}O_{17}:Eu^{2+}$ (BAM:Eu^{2+}) and green $(Sr,Ba)_2SiO_4:Eu^{2+}$ phosphors on the surface of a NUV InGaN chip (λ = 395 nm). Under application of 20 mA (3.245 V) current, the white light with CIE color coordinates of (0.3842, 0.3908), T_c of 4000 K and R_a of 90 was obtained (Fig. 10a and b). The R_a value is higher than that of the *w*-LED devices fabricated with $Ca_3Gd(AlO)_3(BO_3)_4:Eu^{3+}$ red phosphors (Ra = 72.5) [62]. Furthermore, the chromaticity parameters of the as-prepared *w*-LED operated in different currents were measured (Table S5), and little changes for the correlation parameters were observed with increasing the current.

4. Conclusions

The pure red-emitting RBPWO:Eu^{3+} phosphors with high thermal stability and high quantum efficiency were synthesized. The RBPWO:Eu^{3+} phosphors exhibit strong and broad CT absorption band centred at 260 nm and narrow absorption peak with

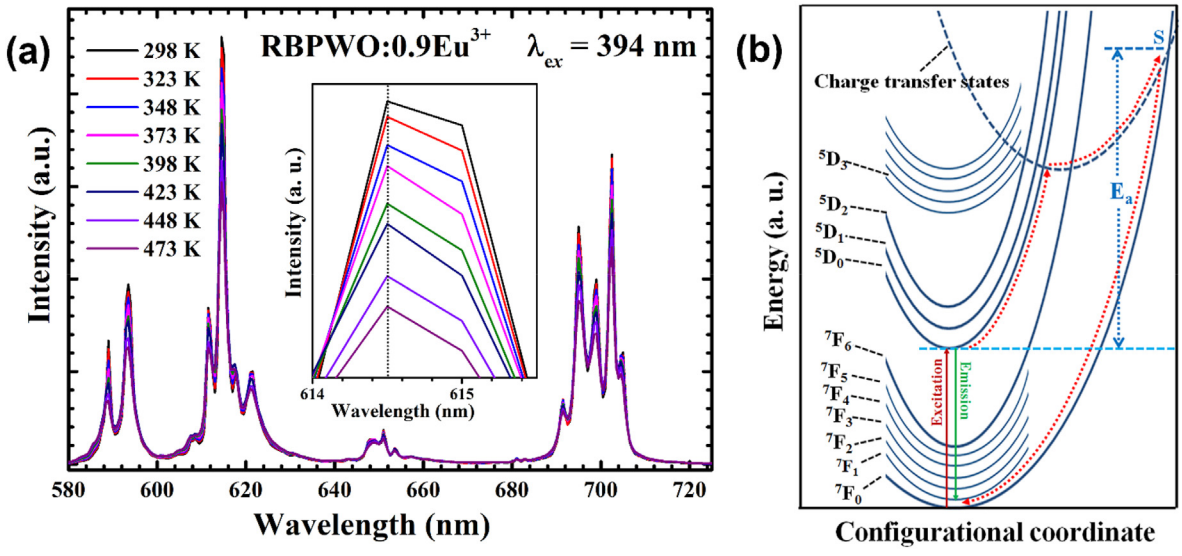

Fig. 9. (a) Variable-temperature photoluminescence spectra, and (b) Configuration coordinate diagram to show the process of thermal quenching of RBPWO:0.9Eu^{3+}.

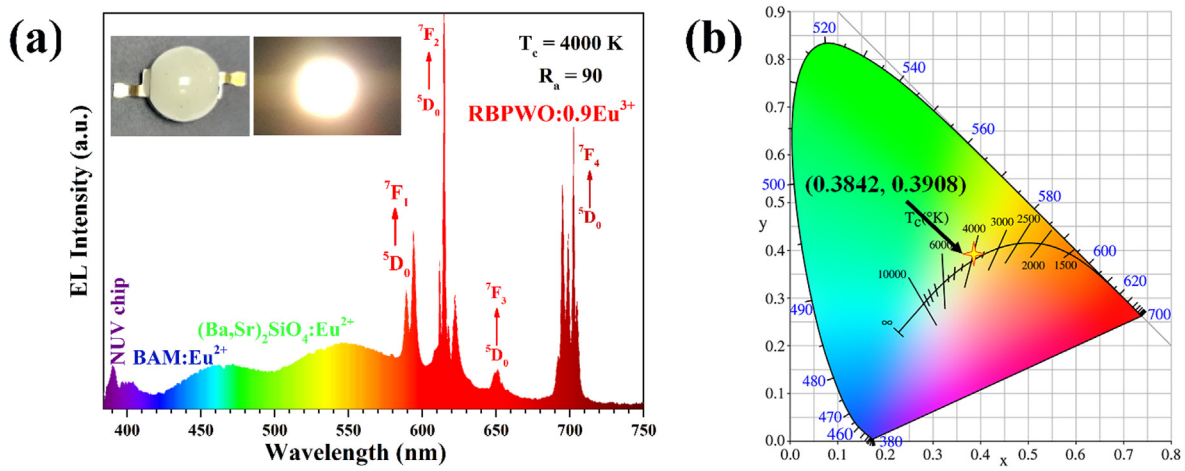

Fig. 10. (a) the electroluminescence spectrum (inset shows the fabricated device), and (b) the CIE chromaticity diagram with the coordinates of *w*-LED device fabricated with a 395 nm NUV chip.

maximum at 394 nm. The phosphors show intense red photoluminescence due to the $^5D_0$-$^7F_2$ transition dominating the emission spectra. Under the excitation at 394 nm, the AQY values can reach up to 88.1%. The total output lights almost invariable until the ambient temperature is higher than 423 K. The fabricated *w*-LED device can generate white light with CIE chromaticity coordinates of (0.3842, 0.3908), T_c of 4000 K and R_a of 90. Therefore, the RBPWO:Eu^{3+} phosphors are expected as newly promising red-emitting components for application in *w*-LEDs.

CRediT authorship contribution statement

Zhen Jia: Data curation, Formal analysis, Writing - original draft. **Xiuling Zhang:** Methodology, Data curation. **Xiaoying Hua:** Methodology, Data curation. **Yan Dong:** Methodology, Data curation. **Hongliang Li:** Methodology, Data curation. **Chuanqi Feng:** Methodology, Data curation. **Yonggang Wang:** Formal analysis. **Mingjun Xia:** Methodology, Writing - review & editing.

Declaration of competing interest

The authors declare that they have no known competing financial interests or personal relationships that could have appeared to influence the work reported in this paper.

Acknowledgements

We really appreciate the support of the Open Project Program of Key Laboratory of Functional Crystals and Laser Technology, TIPC, CAS (FCLT201704), the Training Programs of Innovation and Entrepreneurship for Undergraduates of Shandong Province (201910448036).

Appendix A. Supplementary data

Supplementary data to this article can be found online at https://doi.org/10.1016/j.jallcom.2020.155875.

References

[1] X.L. Liu, Z. Song, S.Y. Zhang, Z.G. Xia, Q.L. Liu, Structure and photoluminescence properties of $Ca_{0.99-x}Sr_xAlSiN_3$:0.01Ce^{3+} solid solutions, J. Am. Ceram. Soc. 102 (2019) 4648–4658.
[2] J.W. Qiao, L.X. Ning, M.S. Molokeev, Y.C. Chuang, Q.Y. Zhang, K.R. Poeppelmeier, Z.G. Xia, Site-selective occupancy of Eu^{2+} toward blue-light-excited red emission in a $Rb_3YSi_2O_7$:Eu phosphor, Angew. Chem. Int. Ed. 58 (2019) 11521–11526.
[3] J.W. Qiao, G.J. Zhou, Y.Y. Zhou, Q.Y. Zhang, Z.G. Xia, Divalent europium-doped near-infrared-emitting phosphor for light-emitting diodes, Nat. Commun. 10 (2019) 5267.
[4] M.I. Nathan, The blue laser diode: GaN based light emitters and lasers, Science 277 (1997) 46–47.
[5] V.V. Atuchin, N.F. Beisel, E.N. Galashov, E.M. Mandrik, M.S. Molokeev, A.P. Yelisseyev, A.A. Yusuf, Z. Xia, Pressure-stimulated synthesis and luminescence properties of microcrystalline $(Lu,Y)_3Al_5O_{12}:Ce^{3+}$ garnet phosphors, ACS Appl. Mater. Interfaces 7 (2015) 26235–26243.
[6] H.P. Ji, L. Wang, M.S. Molokeev, N. Hirosaki, R.J. Xie, Z.H. Huang, Z.G. Xia, O.M. ten Kate, L.H. Liu, V.V. Atuchin, Structure evolution and photoluminescence of $Lu_3(Al,Mg)_2(Al,Si)_3O_{12}:Ce^{3+}$ phosphors: New yellow-color converters for blue LED-driven solid state lighting, J. Mater. Chem. C. 4 (2016) 6855–6863.
[7] E.N. Galashov, V.V. Atuchin, T.A. Gavrilova, I.V. Korolkov, Y.M. Mandrik, A.P. Yelisseyev, Z.G. Xia, Synthesis of $Y_3Al_5O_{12}:Ce^{3+}$ phosphor in the Y_2O_3-Al metal-CeO_2 ternary system, J. Mater. Sci. 52 (2017) 13033–13039.
[8] J. Qiao, J. Zhao, Q. Liu, Z. Xia, Recent advances in solid-state LED phosphors with thermally stable luminescence, J. Rare Earths 37 (2019) 565–572.
[9] H.D. Nguyen, C.C. Lin, R.S. Liu, Waterproof alkyl phosphate coated fluoride phosphors for optoelectronic materials, Angew. Chem. Int. Ed. 54 (2015) 10862–10866.
[10] M. Zhao, H. Liao, L. Ning, Q. Zhang, Q. Liu, Z. Xia, Next-generation narrow-band green-emitting $RbLi(Li_3SiO_4)_2:Eu^{2+}$ phosphor for backlight display application, Adv. Mater. (2018) e1802489.
[11] L. Sun, B. Devakumar, J. Liang, S. Wang, Q. Sun, X. Huang, Highly efficient Ce^{3+} > Tb^{3+} energy transfer induced bright narrowband green emissions from garnet-type $Ca_2YZr_2(AlO_4)_3:Ce^{3+},Tb^{3+}$ phosphors for white LEDs with high color rendering index, J. Mater. Chem. C. 7 (2019) 10471–10480.
[12] L. Sun, B. Devakumar, J. Liang, S. Wang, Q. Sun, X. Huang, A broadband cyan-emitting $Ca_2LuZr_2(AlO_4)_3:Ce^{3+}$ garnet phosphor for near-ultraviolet-pumped warm-white light-emitting diodes with an improved color rendering index, J. Mater. Chem. C. 8 (2020) 1095–1103.
[13] J. Liang, B. Devakumar, L. Sun, S. Wang, Q. Sun, X. Huang, Full-visible-spectrum lighting enabled by an excellent cyan-emitting garnet phosphor, J. Mater. Chem. C. 8 (2020) 4934–4943.
[14] X.Q. Piao, T. Horikawa, H. Hanzawa, K. Machida, Characterization and luminescence properties of $Sr_2Si_5N_8:Eu^{2+}$ phosphor for white light-emitting-diode illumination, Appl. Phys. Lett. 88 (2006) 161908.
[15] Y.S. Kim, S.W. Choi, J.H. Park, E. Bok, B.K. Kim, S.H. Hong, Red-emitting (Sr,Ca) $AlSiN_3:Eu^{2+}$ phosphors synthesized by spark plasma sintering, Ecs. J. Solid. State Sc. 2 (2013) R3021–R3025.
[16] J.D. Axe, P.F. Weller, Fluorescence energy transfer in $Y_2O_3:Eu_{3+}$, J. Chem. Phys. 40 (1964) 3066–3069.
[17] C.I. Jeon, S.I. Mho, Q.W. Choi, C.H. Kim, The formation process of Y_2O_2S-Eu^{3+}, a red phosphor, J. Electrochem. Soc. 135 (1988) C390.
[18] Z.G. Xia, Y.Y. Zhang, M.S. Molokeev, V.V. Atuchin, Structural and luminescence properties of yellow-emitting $NaScSi_2O_6:Eu^{2+}$ phosphors: Eu^{2+} site preference analysis and generation of red emission by codoping Mn^{2+} for white-light-emitting diode applications, J. Phys. Chem. C 117 (2013) 20847–20854.
[19] H. Ji, Z. Huang, Z. Xia, M.S. Molokeev, V.V. Atuchin, M. Fang, Y. Liu, Discovery of New solid solution phosphors via cation substitution-dependent phase transition in $M_3(PO_4)_2:Eu^{2+}$ (M = Ca/Sr/Ba) quasi-binary sets, J. Phys. Chem. C 119 (2015) 2038–2045.
[20] H. Ji, Z. Huang, Z. Xia, M.S. Molokeev, X. Jiang, Z. Lin, V.V. Atuchin, Comparative

investigations of the crystal structure and photoluminescence property of eulytite-type $Ba_3Eu(PO_4)_3$ and $Sr_3Eu(PO_4)_3$, Dalton Trans. 44 (2015) 7679–7686.
[21] R.S. Liu, Up Conversion Nano Particles, Quantum Dots and Their Applications, Springer, 2016.
[22] V.V. Atuchin, A.S. Aleksandrovsky, O.D. Chimitova, T.A. Gavrilova, A.S. Krylov, M.S. Molokeev, A.S. Oreshonkov, B.G. Bazarov, J.G. Bazarova, Synthesis and spectroscopic properties of monoclinic alpha-$Eu_2(MoO_4)_3$, J. Phys. Chem. C 118 (2014) 15404–15411.
[23] P. Shi, Z. Xia, M.S. Molokeev, V.V. Atuchin, Crystal chemistry and luminescence properties of red-emitting $CsGd_{1-x}Eu_x(MoO_4)_2$ solid-solution phosphors, Dalton Trans. 43 (2014) 9669–9676.
[24] K. Binnemans, Interpretation of europium (III) epectra, Coord. Chem. Rev. 295 (2015) 1–45.
[25] Y.G. Denisenko, V.V. Atuchin, M.S. Molokeev, A.S. Aleksandrovsky, A.S. Krylov, A.S. Oreshonkov, S.S. Volkova, O.V. Andreev, Structure, thermal stability, and spectroscopic properties of triclinic double sulfate $AgEu(SO_4)_2$ with isolated SO_4 groups, Inorg. Chem. 57 (2018) 13279–13288.
[26] P. Dorenbos, The Eu^{3+} charge transfer energy and the relation with the band gap of compounds, J. Lumin. 111 (2005) 89–104.
[27] R.D. Shannon, Revised effective ionic radii and systematic studies of interatomie distances in halides and chaleogenides, Acta Crystallogr. 32 (1976) 751–767.
[28] Z. Gao, P. Sun, Y. Zhong, R. Yu, B. Deng, Eu^{3+} doped highly thermal-stable barium yttrium aluminate as a red-emitting phosphor for UV based white white LED, Optic Laser. Technol. 111 (2019) 163–168.
[29] J.Y. Park, J.W. Chung, S.J. Park, H.K. Yang, Versatile fluorescent $CaGdAlO_4:Eu^{3+}$ red phosphor for latent fingerprints detection, J. Alloys Compd. 824 (2020) 153994.
[30] M. Rajendran, S. Vaidyanathan, New red emitting phosphors $NaSrLa(MO_4)_3:Eu^{3+}$ M = Mo and W for white LEDs: synthesis, structural and optical study, J. Alloys Compd. 789 (2019) 919–931.
[31] J. Dalal, M. Dalal, S. Devi, A. Hooda, A. Khatkar, V.B. Taxak, S.P. Khatkar, Radiative and non-radiative characteristics of $Ca_9Bi(PO_4)_7:Eu^{3+}$ nanophosphor for solid state lighting devices, J. Lumin. 216 (2019) 116697.
[32] M.J. Xia, R.K. Li, Crystal structure and characterization of mixed anion compounds $Rb_2Bi(PO_4)(MO_4)$ (M = Mo, W), Solid State Commun. 201 (2015) 102–106.
[33] G. Blasse, The Influence of Charge-Transfer and Rydberg States on the Luminescence Properties of Lanthanides and Actinides, Springer, 1976.
[34] X. Zhang, M. Chen, J. Zhang, X. Qin, M. Gong, Photoluminescence studies of high-efficient red-emitting $K_2Y(WO_4)(PO_4):Eu^{3+}$ phosphor for NUV LED, Mater. Res. Bull. 73 (2016) 219–225.
[35] X. Huang, B. Li, H. Guo, Highly efficient Eu^{3+}-activated $K_2Gd(WO_4)(PO_4)$ red-emitting phosphors with superior thermal stability for solid-state lighting, Ceram. Int. 43 (2017) 10566–10571.
[36] X. Huang, H. Guo, B. Li, Eu^{3+}-activated $Na_2Gd(PO_4)(MoO_4)$: a novel high-brightness redemitting phosphor with high color purity and quantum efficiency for white light-emitting diodes, J. Alloys Compd. 720 (2017) 29–38.
[37] H. Guo, X. Huang, Low-temperature solid-state synthesis and photoluminescence properties of novel high-brightness and thermal-stable Eu^{3+}-activated $Na_2Lu(MoO_4)(PO_4)$ red-emitting phosphors for near-UV-excited white LEDs, J. Alloys Compd. 764 (2018) 809–814.
[38] J. Grigorjevaite, E. Ezerskyte, A. Minderyte, S. Stanionyte, R. Juskenas, S. Sakirzanovas, A. Katelnikovas, Optical properties of red-emitting $Rb_2Bi(PO_4)(MoO_4):Eu^{3+}$ powders and ceramics with high quantum efficiency for white LEDs, Materials 12 (2019) 3275.
[39] B.H. Toby, EXPGUI, A graphical user interface for GSAS, J. Appl. Crystallogr. 34 (2001) 210–213.
[40] A. C. Larson, R. B. Von Dreele. Genernal structure analysis system (GSAS). Los Alamos National Laboratory Report LAUR 86-748: 2004.
[41] H.M. Rietveld, Line profiles of neutron powder diffraction peaks for structure refinement, Acta Crystallogr. 22 (1967) 151–152.
[42] H.M. Rietveld, A profile refinement method for nuclear and magnetic structures, J. Appl. Crystallogr. 2 (1969) 65–71.
[43] V.V. Atuchin, O.D. Chimitova, T.A. Gavrilova, M.S. Molokeev, S.J. Kim, N.V. Surovtsev, B. G. Bazarov Synthesis, Structural and vibrational properties of microcrystalline $RbNd(MoO_4)_2$, J. Cryst. Growth 318 (2011) 683–686.
[44] V.V. Atuchin, O.D. Chimitova, S.V. Adichtchev, J.G. Bazarov, T.A. Gavrilova, M.S. Molokeev, N.V. Surovtsev, Z. G. Bazarova Synthesis, Structural and vibrational properties of microcrystalline beta-$RbSm(MoO_4)_2$, Mater. Lett. 106 (2013) 26–29.
[45] O.D. Chimitova, V.V. Atuchin, B.G. Bazarov, M.S. Molokeev, Z.G. Bazarova, The formation and structural parameters of new double molybdates $RbLn(MoO_4)_2$ (ln = Pr, Nd, Sm, Eu), in: V. Kuzmiak, P. Markos, T. Szoplik (Eds.), Metamaterials Viii,, 8771, Proc. SPIE, 2013, 87711A.
[46] R.D. Shannon, C.T. Prewitt, Effective ionic radii in oxides and fluorides, Acta Crystallogr. B25 (1968) 925–946.
[47] R.D. Shannon, C.T. Prewitt, Effective ionic radii in oxides and fluorides, Acta Crystallogr. B 25 (1969) 925–946.
[48] P. Kubelka, F. Munk, Ein beitrag zur optik der farbanstriche, Z. Tech. Phys. 12 (1931) 593–601.
[49] P. Dorenbos, Valence stability of lanthanide ions in inorganic compounds, Chem. Mater. 17 (2017) 6452–6456.
[50] G.S. Ofelt, Structure of F_6 configuration with application to rare-earth ions, J. Chem. Phys. 38 (1963) 2171–2180.
[51] V.V. Atuchin, A.K. Subanakov, A.S. Aleksandrovsky, B.G. Bazarov, J.G. Bazarova, T.A. Gavrilova, A.S. Krylov, M.S. Molokeev, A.S. Oreshonkov, S.Y. Stefanovich, Structural and spectroscopic properties of new noncentrosymmetric self-activated borate $Rb_3EuB_6O_{12}$ with B_5O_{10} units, Mater. Des. 140 (2018) 488–494.
[52] V.V. Atuchin, A.S. Aleksandrovsky, B.G. Bazarov, J.G. Bazarova, O.D. Chimitova, Y.G. Denisenko, T.A. Gavrilova, A.S. Krylov, E.A. Maximovskiy, M.S. Molokeev, A.S. Oreshonkov, A.M. Pugachev, N.V. Surovtsev, Exploration of structural, vibrational and spectroscopic properties of self-activated orthorhombic double molybdate $RbEu(MoO_4)_2$ with isolated MoO_4 units, J. Alloys Compd. 785 (2019) 692–697.
[53] G. Blasse, A. Bril, W. Nieuwpoo, On Eu^{3+} fluorescence in mixed metal oxides. 1. Crystal structure sensitivity of intensity ratio of electric and magnetic dipole emission, J. Phys. Chem. Solid. 27 (1966) 1587–1592.
[54] L.L. Sun, H. Guo, J. Liang, B. Li, X.Y. Huang, $Ca_3Lu(GaO)_3(BO_3)_4:Eu^{3+}$: a novel high-brightness and thermal-stable red-emitting phosphor for white LEDs, J. Lumin. 202 (2018) 403–408.
[55] H. Guo, L.L. Sun, J. Liang, B. Li, X.Y. Huang, High-efficiency and thermal-stable Eu^{3+}-activated $Ca_3Y(AlO)_3(BO_3)_4$ red-emitting phosphors for near-UV-excited white LEDs, J. Lumin. 205 (2019) 115–121.
[56] J.E. Lowther, Spectroscopic transition-probabilities of rare-earth ions, J. Phys. C: Solid. State. 7 (1974) 4393–4402.
[57] G. Blasse, Energy transfer in oxidic phosphors, Philips Res. Rep. 24 (1969) 131–144.
[58] Y.C. Chang, C.H. Liang, S.A. Yan, Y.S. Chang, Synthesis and photoluminescence characteristics of high color purity and brightness $Li_3Ba_2Gd_3(MoO_4)_8:Eu^{3+}$ red phosphors, J. Phys. Chem. C 114 (2010) 3645–3652.
[59] H. Guo, X.Y. Huang, Y.J. Zeng, Synthesis and photoluminescence properties of novel highly thermal-stable red-emitting $Na_3Sc_2(PO_4)_3:Eu^{3+}$ phosphors for UV-excited white-light-emitting diodes, J. Alloys Compd. 741 (2018) 300–306.
[60] B. Tian, B. Chen, Y. Tian, X. Li, J. Zhang, J. Sun, H. Zhong, L. Cheng, S. Fu, H. Zhong, Y. Wang, X. Zhang, H. Xia, R. Hu, Excitation pathway and temperature dependent luminescence in color tunable $Ba_5Gd_8Zn_4O_{21}:Eu^{3+}$ phosphors, J. Mater. Chem. C. 1 (2013) 2338–2344.
[61] A. Katelnikovas, J. Plewa, S. Sakirzanovas, D. Dutczak, D. Enseling, F. Baur, H. Winkler, A. Kareiva, T. Juestel, Synthesis and optical properties of $Li_3Ba_2La_3(MoO_4)_8:Eu^{3+}$ powders and ceramics for pcLEDs, J. Mater. Chem. 22 (2012) 22126–22134.
[62] B. Li, S. Wang, Q. Sun, C. Lu, H. Guo, X. Huang, Novel high-brightness and thermal-stable $Ca_3Gd(AlO)_3(BO_3)_4:Eu^{3+}$ red phosphors with high colour purity for NUV-pumped white LEDs, Dyes Pigments 154 (2018) 252–256.